EES Catalysis

PAPER

View Article Online
View Journal | View Issue

Cite this: *EES Catal.*, 2025, 3, 535

CO_2/NO_x storage and reduction (CNSR) technology—a new concept for flue gas treatment†

Jiaqi Wei,[ab] Yanshan Gao,*[ab] Cheng Zhang[ab] and Qiang Wang*[ab]

Received 31st October 2024,
Accepted 26th February 2025

DOI: 10.1039/d4ey00235k

rsc.li/eescatalysis

The emission of CO_2 and NO_x from industrial factories poses significant challenges to human health and contributes to extreme climate change. NO_x storage and reduction (NSR) and integrated CO_2 capture and methanation (ICCM) technology are some of the effective technologies used to deal with NO_x and CO_2, respectively. However, there is currently no relevant technology available for the simultaneous removal of both NO_x and CO_2 gases co-existing in flue gas. This paper proposes a new concept named CO_2/NO_x storage and reduction (CNSR) for the first time. This approach utilizes a K–Pt/$Ni_3Al_1O_x$ dual functional material (DFM) to achieve co-storage of CO_2 and NO_x, followed by their reduction to CH_4 and N_2, respectively. The CNSR tests demonstrate the feasibility of this technology. At 350 °C, the conversion for CO_2 and NO_x was 60.8% and 99.5%, with CH_4 and N_2 selectivity of 98.9% and 90.3%, respectively. After 10 cycles, the sample exhibited a relatively stable CO_2 conversion of around 66%, with CH_4 selectivity remaining above 90%. The conversion of NO_x remained essentially unchanged at close to 100%. Furthermore, a possible mechanism for the CNSR process is proposed in this study. We believe that this work will provide a novel strategy for the treatment of multi-component gaseous pollutants in flue gas.

Broader context

Emissions of CO_2 and NO_x pose significant environmental challenges, driving research into removal technologies such as NO_x storage and reduction (NSR) for NO_x removal and integrated CO_2 capture and methanation (ICCM) for CO_2. While both areas are advancing rapidly, the simultaneous removal of NO_x and CO_2 gases co-existing in flue gas remains a challenge due to the complex reaction conditions. Effective system design and development of bifunctional materials are crucial to overcome these challenges. In this work, a new concept named CO_2/NO_x storage and reduction (CNSR) is proposed for the first time and a suitable dual functional material (DFM), K–Pt/$Ni_3Al_1O_x$, is designed for this innovative process. The designed K–Pt/$Ni_3Al_1O_x$ DFM demonstrated promising CNSR performance, highlighting the feasibility of CNSR. The speculative mechanism for the process over K–Pt/$Ni_3Al_1O_x$ DFM was proposed. This research offers a new strategy for the removal and recycling of CO_2 and NO_x in flue gas, paving the way for carbon-negative emissions.

1. Introduction

Due to the rising energy demands, the increased emissions of gaseous pollutants into the environment is still a big challenge.[1] Although replacing fossil fuels with renewable energy and bioenergy can help reduce carbon emissions, over 80% of the energy supply in China still relies on traditional sources, including coal, oil and natural gas.[2] The combustion of these fuels releases carbon dioxide (CO_2), often accompanied by nitrogen oxide (NO_x), which poses significant threats to both the ecological environment and human health.[3] Furthermore, as direct and indirect contributors to greenhouse gases, CO_2 and NO_x have detrimental effects on the global climate.[4]

Over the past few decades, various technologies for NO_x control have been continuously explored and developed.[5–8] Among these, the concept of NO_x storage and reduction (NSR), first proposed by Naoki Takahashi,[9] involves a process in which NO_x is stored on alkaline components under oxidizing conditions and then converted into nitrogen under reducing conditions. In terms of CO_2 capture, Duyar *et al.*[10] designed an innovative process that integrates CO_2 capture with the methanation process, known as integrated CO_2 capture and methanation (ICCM). This process eliminates the limitations of

[a] College of Environmental Science and Engineering, Beijing Forestry University, Beijing 100083, China. E-mail: yanshan_gao@bjfu.edu.cn, qiangwang@bjfu.edu.cn
[b] State Key Laboratory of Efficient Production of Forest Resources, Beijing Forestry University, Beijing 100083, China

† Electronic supplementary information (ESI) available. See DOI: https://doi.org/10.1039/d4ey00235k

traditional carbon capture and storage (CCS) or carbon capture and utilization (CCU) technologies, which are constrained by high energy consumption and costs associated with separation and logistics.[11,12] Recently, Porta *et al.*[13] provided valuable insights into the role and interplay of CO_2 storage and hydrogenation functions in the Ru–BaO/Al_2O_3 dual functional material (DFM) for CO_2 capture from exhaust flue gases. Additionally, sulfur tolerance and the self-regeneration mechanism of Na(Li)–Ru/Al_2O_3 DFM for the integrated CO_2 capture and methanation were systematically investigated by Cimino *et al.*[14,15] The findings demonstrated that the CO_2 capture and methanation process exhibited significant tolerance to high concentrations of SO_2, due to the self-regeneration mechanism of the Ru catalytic sites. In addition to the ICCM reaction, other ICCU technologies can be realized by adjusting factors such as reaction temperature, catalysts, reducing agents, and other parameter conditions. For example, CO_2 capture can be coupled with reactions like the reverse water gas shift (ICCU-RWGS) and methane dry reforming (ICCU-DRM).[16–18] Furthermore, other conversion products in ICCU, such as methanol, are actively being explored. For example, unlike conventional ICCU using solid-state DFMs, efficient CO_2 conversion can be achieved by combining solution-phase CO_2 capture with solid-state catalysts. Kothandaraman *et al.*[19] demonstrated excellent methanol selectivity (70%) by using 2-EEMPA as a CO_2 solvent combined with a Pt/TiO_2 catalyst. Additionally, Sen *et al.*[20] developed the first ICCU system using alkali hydroxide solutions (*e.g.*, NaOH, KOH) for CO_2 capture, which was subsequently converted to CH_3OH *via* Ru–PNP catalysts. This integration also offers a promising route for efficient CO_2 utilization.

Although the NSR and ICCM technologies can achieve efficient removal of NO_x and CO_2, respectively, for the co-existence of NO_x and CO_2 in flue gas, there is currently no relevant technology available for their simultaneous removal. Therefore, exploring an integrated approach that leverages the strength of these two technologies can achieve simultaneous removal of NO_x and CO_2. In this contribution, to achieve simultaneous removal of NO_x and CO_2 in flue gas, an innovative concept is proposed: CO_2 and NO_x storage and reduction (CNSR) technology. The general working principal of CNSR is illustrated in Scheme 1. In the first stage, CO_2 and NO_x from flue gases are captured by the adsorptive components of DFMs (storage process). In the second stage, green H_2, produced through renewable energy-driven electrolysis, reduces the adsorbed species to CH_4 and N_2 *via* a catalyst (reduction process). The ultimate goal is to achieve efficient collaborative removal of CO_2 and NO_x, thereby realizing zero-carbon emissions and pollutant elimination.

The key to CNSR technology lies in the development of DFMs that incorporate both adsorption sites and catalytic sites. For the selection of adsorptive components, Na_2O and K_2O produced from the hydrogenation of carbonate precursors, are considered excellent choices for the ICCM process.[21] Meanwhile, K species have been found to be more effective for the NSR process in the medium to high-temperature region (>300 °C) compared to the traditional Ba species.[22,23] Regarding the catalytic component, Ni is well established for both methanation and ICCM reactions due to its low price and excellent activity.[24–28] In addition, to assist the catalytic performance of Ni, precious metals can be incorporated to accelerate the multiple reaction processes.[29] Particularly, platinum-group metals are promising for NO oxidation, nitrate reduction, and CO_2 methanation.[30,31]

Herein, a new concept named CO_2/NO_x storage and reduction (CNSR) is proposed for the first time and a suitable DFM of K–Pt/$Ni_3Al_1O_x$ was designed for this innovative process. The performance of K–Pt/$Ni_3Al_1O_x$ for the separate ICCM and NSR reactions as well as its feasibility for the CNSR process was thoroughly evaluated. The involved reaction mechanisms of

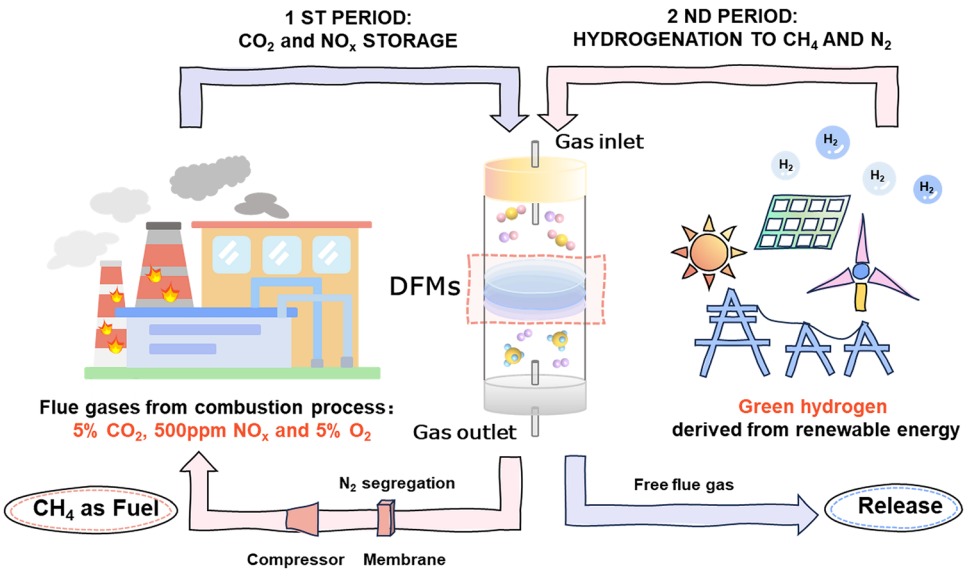

Scheme 1 A scheme of the CO_2/NO_x storage and reduction (CNSR) technology.

this innovative CNSR process were revealed. This study aims to pioneer a new technology of CNSR for the simultaneous treatment of CO_2 and NO_x in flue gases.

2. Experimental section

2.1 Preparation of K–Pt/$Ni_3Al_1O_x$

NiAl–CO_3 layered double hydroxides (LDHs) were fabricated by a co-precipitation method with aqueous miscible organic (AMO) treatment.[32] Briefly, a 100 mL Ni–Al precursor solution consisting of 0.075 mol $Ni(NO_3)_2{\cdot}6H_2O$ and 0.025 mol $Al(NO_3)_3{\cdot}9H_2O$, was added dropwise to a 100 mL precipitant solution containing 0.05 mol of Na_2CO_3 under stirring at 500 rpm. During this process, the pH value was controlled at approximately 10 ± 0.5 using a 4 M NaOH solution. The resulting suspension was aged for 24 h with vigorous agitation at room temperature, then filtered with deionized water until the filtrate was neutral, followed by rinsing with ethanol. Subsequently, the solid-phase was redispersed in ethanol and stirring for 2 h. The filter cake was collected by filtration and dried overnight in an oven at 60 °C, and then labeled as Ni_3Al_1-LDH after grinding. Finally, the dried LDH powder was calcined at 500 °C for 5 h to obtain $Ni_3Al_1O_x$.

K–Pt/$Ni_3Al_1O_x$ was synthesized using a successive impregnation method. First, H_2PtCl_6 ethanol solution and K_2CO_3 aqueous solution were prepared. The obtained $Ni_3Al_1O_x$ powders were then impregnated with the H_2PtCl_6 ethanol solution, followed by stirring for 2 h. The mixture was poured into a rotary evaporator until ethanol was completely volatilized. The obtained powder was calcined at 500 °C for 5 h and referred to as Pt/$Ni_3Al_1O_x$. Subsequently, the Pt/$Ni_3Al_1O_x$ samples were impregnated with the K_2CO_3 aqueous solution, and the aforementioned procedure was repeated. The theoretical loadings of Pt and K_2CO_3 were set at 1 wt% and 10 wt%, respectively. The final obtained samples were denoted as K–Pt/$Ni_3Al_1O_x$. The detailed synthesis process is illustrated in Fig. 1a. Specially, the suffix '–R' is used to represent the reduced samples.

2.2 Characterization of materials

X-ray diffraction (XRD) tests were carried out on Shimadzu XRD-7000 equipment with Cu Kα radiation. The operating range for 2θ was set from 5° to 80°, with a scanning speed of 5 °C min^{-1} and a step size of 0.02°. The porosity properties of all calcined and reduced catalysts were determined using a Builder SSA-7000 instrument following the BET method. The Pt and K contents for K–Pt/$Ni_3Al_1O_x$ were measured using an inductively coupled plasma optical emission spectrometer (ICP-OES, Shimadzu ICPE-9800). The microstructure was observed using high-resolution transmission electron microscopy (HR-TEM, JEM-2100F, JEOL) at an accelerating voltage of 200 kV. X-ray photoelectron spectroscopy (XPS) was performed for valence analysis on Thermo Escalab 250Xi equipment with Al Kα radiation (1486.6 eV).

Temperature-programmed reduction and desorption (TPR and TPD) experiments were conducted on a chemical adsorption instrument (PCA-1200). A 0.1 g sample was loaded in a quartz tube and underwent pretreatment prior to testing. Two modes of pretreatment were employed: one is pretreated with Ar at 500 °C for 1 h, while the other involved reduced with a 5% H_2/Ar (when used) at 500 °C for 2 h, followed by cooling to 50 °C. For H_2-TPR, all samples were pretreated with Ar before being heated from 50 °C to 800 °C under a flow of 5% H_2/Ar. The reduction signal was monitored by TCD detector. In CO_2-TPD, the well-pretreated samples were saturated by adsorbing pure CO_2 for 1 h at 50 °C, followed by a switch to Ar to sweep away weakly physisorbed CO_2 while stabilizing the voltage. The desorption curve was then recorded using a TCD detector with temperature rising from 50 °C to 800 °C in an Ar stream. Similarly, the NO-TPD experiments were operated in the same manner, with the adsorption gas changed to 1% NO/Ar. During the TPR and TPD process, the gas flow rate was maintained at 30 mL min^{-1}, and the heating rate was set to 10 °C min^{-1}.

A temperature-programmed hydrogenation (TPH) test was arranged to detect the hydrogenation products of K–Pt/$Ni_3Al_1O_x$, with the same procedure as H_2-TPR. The reaction off-gas components of CH_4 and CO_2 were recorded continuously by mass spectrometry (MS). These components were identified by their distinct mass-to-charge ratios, with m/z values of 15 for CH_4 and 44 for CO_2.

In situ diffuse reflectance infrared transform spectroscopy (DRIFTS) experiments were conducted using a Fourier transform infrared spectrometer (FT-IR, Spectrum 3, PerkinElmer), equipped with a liquid N_2 cooled MCT detector at 4 cm^{-1} resolution averaging over 16 scans. The *in situ* DRIFT measurements were carried out in a sealed high-temperature cell equipped with ZnSe windows. To observe the changes during the pre-reduction process of K–Pt/$Ni_3Al_1O_x$, the sample was treated with Ar at 500 °C for 1 h to remove moisture and impurities on the surface. After this treatment, the sample was cooled to 50 °C and then switched to 5% H_2/Ar. At this point, the IR spectrum was scanned and used as the background. Afterwards, the temperature was increased from 50 °C to 500 °C with a heating rate of 10 °C min^{-1} and maintained at 500 °C for 30 min. During this process, the spectrum was recorded at 50 °C intervals from 50 °C up to 500 °C. After reaching 500 °C, additional scans were conducted at 10-min intervals to monitor changes in the spectrum. Additionally, to explore the reaction process of CNSR, the K–Pt/$Ni_3Al_1O_x$ powder was pre-reduced at 500 °C under 25% H_2/Ar for 1 h before each experiment. The temperature was then cooled down to 350 °C and the background was collected. Three adsorption–reduction modes were performed by adjusting the gas composition during the adsorption period: (1) 5% CO_2/5% O_2/Ar for ICCM reaction; (2) 500 ppm NO_x/5% O_2/Ar for NSR reaction; and (3) 5% CO_2/500 ppm NO_x/5% O_2/Ar for CNSR reaction. After 5 min of adsorption, Ar was passed through for a 2-min purge, followed by 15 min of hydrogenation using 25% H_2/Ar. The gas mixture flow rate was 50 mL min^{-1}, and the IR spectra were recorded every 30 s from 700 to 4000 cm^{-1}.

H_2 temperature-programmed surface reaction (H_2-TPSR) was performed to explore the reactivity of CO_2 or NO_x

with H_2. A 0.1 g sample was reduced in a 5% H_2/Ar stream (50 mL min^{-1}) at 500 °C for 2 h, after which the samples were stabilized at the adsorption temperature with Ar (50 °C for CO_2 and 350 °C for and NO_x). Subsequently, the samples were exposed to 5% CO_2/Ar gas stream for 30 min or 500 ppm NO_x/5% O_2/Ar gas stream for 1 h to ensure saturation. After this, Ar was introduced to purge the surface of the samples with decreasing or stabilizing temperature to 50 °C. Finally, the quartz tube was ramped from 50 °C to 800 °C in the stream of 25% H_2/Ar with a flow rate of 50 mL min^{-1}. The outlet gases were monitored by different m/z ratios of 15, 17, 28, 30 and 44, which represent CH_4, NH_3, CO or N_2, NO, and CO_2 or N_2O, respectively.

2.3. Catalytic evaluation of materials

2.3.1 ICCM and NSR performance tests. For both ICCM and NSR tests, a 0.3 g K–Pt/$Ni_3Al_1O_x$ sample was loaded into a vertical tubular stainless steel reactor, carried out using fixed-bed microreactor equipment. Prior to each reaction, the samples underwent a reduction treatment in a 25% H_2 at 500 °C for 2 h. Upon completion of the pre-reduction, the gas was switched from H_2 to Ar at 500 °C for 10 min to purge residual hydrogen from the reactor and catalyst surface. The temperature was then dropped to 350 °C. Each cycle consisted of the following steps: first, the sample was exposed to a gas stream containing 5% CO_2 (or 500 ppm NO_x), 5% O_2, and Ar as a balance for 5 min. And then Ar purge was conducted for 2 min to flush away residual gases from the materials and pipeline. Finally, the post-adsorbed material was fully hydrogenated with 25% H_2 for 15 min.

2.3.2 CNSR performance test. The single-cycle experiment of CNSR was conducted using 0.3 g of K–Pt/$Ni_3Al_1O_x$ sample. The pre-reduction conditions, operational temperature, and reaction time for each stage were consistent with those of ICCM and NSR tests. The only difference in this experiment was the feed composition, which consisted of 5% CO_2, 500 ppm NO_x, 5% O_2, 5% H_2O (when used) and Ar as the dilutant for the CNSR process. The CNSR cycling experiment also included the stages of adsorption (3 min), purge (2 min), hydrogenation (5 min) and re-purge (2 min). Each complete cycle lasted 12 min and was repeated 10 times.

The total gas flow rate for all experiments was set as 200 mL min^{-1}, which corresponds to a WHSV of 40 000 mL g^{-1} h^{-1}. The outlet gases were monitored continuously using an MKS-2000 FTIR spectrometer, which was equipped with a mass flow controller (MFC). The conversions of CO_2 and NO_x, as well as the selectivity of CH_4 and N_2, were calculated using the following eqn (1)–(4).

$$CO_2\ \text{conversion}\ (\%) = \frac{Y_{CH_4} + Y_{CO}}{Y_{CO_2\text{-des}} + Y_{CH_4} + Y_{CO}} \times 100\% \quad (1)$$

$$NO_x\ \text{conversion}\ (\%) = \frac{NO_x\text{-s} - NO_x\text{-des}}{NO_x\text{-s}} \times 100\% \quad (2)$$

$$CH_4\ \text{selectivity}\ (\%) = \frac{Y_{CH_4}}{Y_{CH_4} + Y_{CO}} \times 100\% \quad (3)$$

$$N_2\ \text{selectivity}\ (\%) = \left(1 - \frac{Y_{NH_3} + 2Y_{N_2O}}{NO_x\text{-s} - NO_x\text{-des}}\right) \times 100\% \quad (4)$$

where NO_x-s refers to NO_x storage capacity (NSC); Y_{CH_4}, Y_{CO}, $Y_{CO_2\text{-des}}$, $Y_{NO_x\text{-des}}$, Y_{NH_3} and Y_{N_2O} represent the yield of different products of hydrogenation period, respectively, where their calculation formulas are shown in the ESI.†

3. Results and discussion

3.1. Synthesis and characteristics of novel DFMs

In order to confirm the structures of the materials, XRD analyses of the as-prepared samples were conducted (Fig. 1b). The results revealed distinct diffraction peaks at 2θ = 11.26°, 22.42°, 35.1°, 38.41°, 47.36°, and 61.44° for Ni_3Al-LDH, indicating successful synthesis of the LDH precursor.[33] After calcination at 500 °C, the characteristic peaks of LDH disappeared, and new distinct peaks appeared at 37.2°, 43.5°, 63.2°, and 75.6°. These peaks correspond to the crystal facets of NiO or nickel aluminate spinel.[34] The diffractogram of the reduced K–Pt/$Ni_3Al_1O_x$ sample confirmed the existence of zero-valent nickel, indicated by the emergence of new peaks at 44.6°, 51.9°, and 76.5°, alongside the disappearance of peaks corresponding to nickel oxides.[35] Notably, no peaks corresponding to platinum or potassium species were observed in the XRD patterns of the K–Pt/$Ni_3Al_1O_x$ sample, both before and after reduction. This lack of detection aligns with previous studies, likely due to the platinum content being below the XRD detection limit, while the potassium phase exists in an amorphous and well-dispersed state.[36] But the ICP-OES analysis confirmed the presence of platinum and potassium, with loading amounts of 0.99% and 5.4%, respectively, which are close to the theoretical loading, suggesting successful impregnation of the Pt and K.

The N_2 adsorption–desorption curves of all samples exhibited a typical type IV isotherm along with a H3 hysteresis loop, suggesting the predominance of slit-shaped mesopores (Fig. S1, ESI†).[37] In comparison to the $Ni_3Al_1O_x$ and Pt/$Ni_3Al_1O_x$ samples, the slight decrease in the specific surface area of K–Pt/$Ni_3Al_1O_x$ was ascribed to the pore blockage by the bulky K_2CO_3. However, the specific surface area of hydrogenated K–Pt/$Ni_3Al_1O_x$-R significantly decreased (Table S1, ESI†), likely due to a morphological and structural transformation during reduction, shifting from a fluffy sheet structure to a stacked granular structure, as observed in the TEM image (Fig. 2).

In order to investigate the redox properties of the materials, a H_2-TPR technique was employed. The nickel–aluminum species in the $Ni_3Al_1O_x$ support are uniformly distributed in the form of Ni–O–Al,[38] with a higher proportion of nickel than aluminum. The configuration of Ni^{2+} species predominantly consisted of Ni_2AlO_4, followed by $NiAl_2O_4$, and a small amount of α-NiO, as illustrated in Fig. S2a (ESI†). After Pt loading, the forward shift in the TPR curve is attributed to Pt's ability to

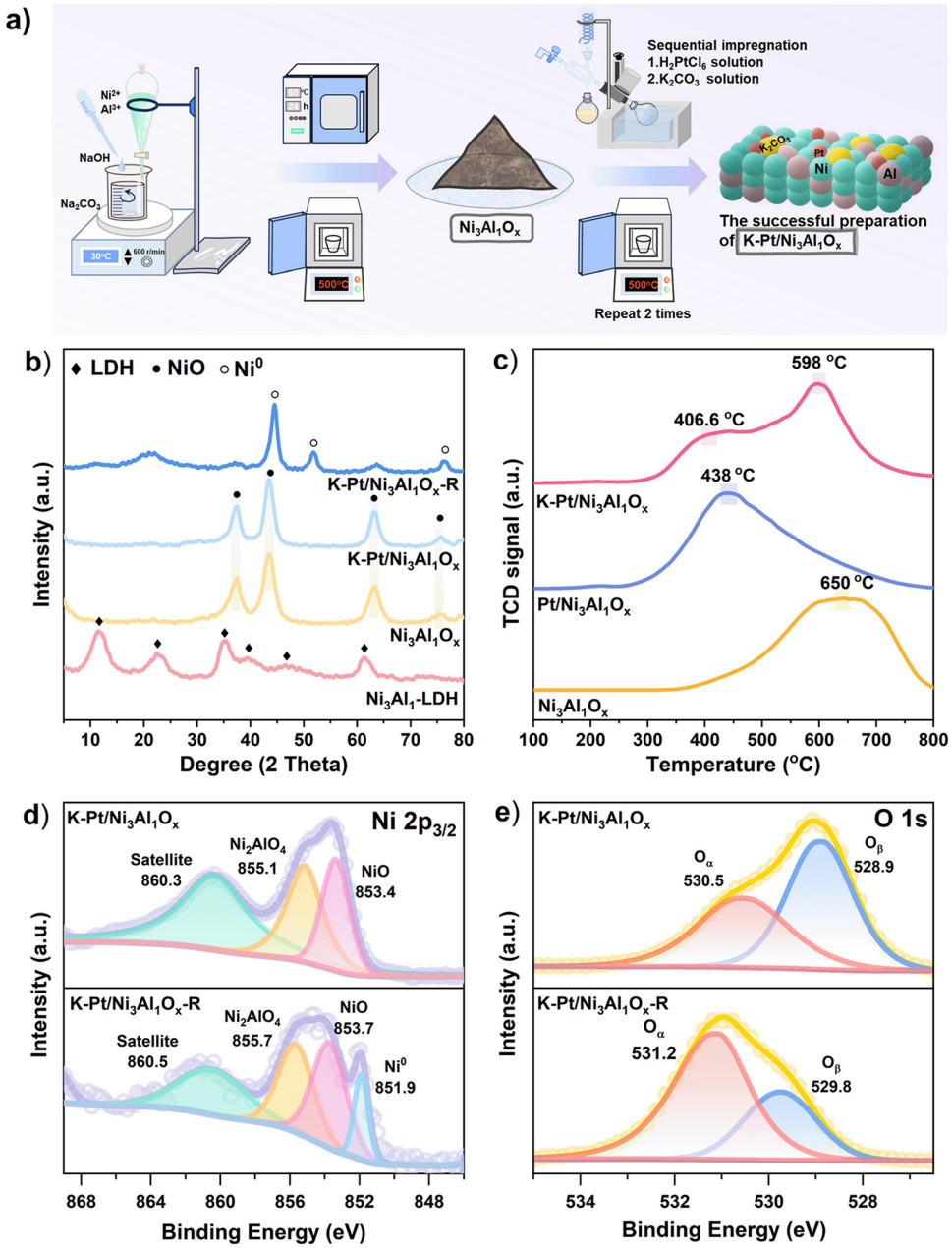

Fig. 1 (a) A schematic diagram of the synthesis route for K–Pt/$Ni_3Al_1O_x$, (b) XRD patterns of all prepared samples, (c) H_2-TPR analyses of $Ni_3Al_1O_x$, Pt/$Ni_3Al_1O_x$ and K–Pt/$Ni_3Al_1O_x$, (d) XPS analyses of Ni $2p_{3/2}$ spectra, and (e) O 1s spectra of K–Pt/$Ni_3Al_1O_x$ and K–Pt/$Ni_3Al_1O_x$-R.

enhance the reducibility of nickel oxides through H dissociation and spillover, thereby lowering the reduction temperature.[39] Besides, a small peak near 200 °C appeared corresponding to the reduction of PtO_x (Fig. S2b, ESI†). However, the presence of K_2CO_3 on the catalysts may cover NiO, hindering H_2 diffusion to NiO.[40] As a result, the reduction peak of K–Pt/$Ni_3Al_1O_x$ shifted to higher temperatures compared to Pt/$Ni_3Al_1O_x$ (Fig. 1c).

Additionally, the total H_2 consumption increased (Table S2, ESI†), suggesting that more hydrogen is being consumed by the K–Pt/$Ni_3Al_1O_x$ sample. This increased H_2 consumption is supported by *in situ* DRIFT and TPH tests. As the temperature increased, inverted peaks in the regional bands associated with carbonate became more pronounced, along with the detection of intermediate species such as CH_3O^* and CHO^*.[41–43] Gaseous CO was also detected in the 300 °C to 400 °C range (Fig. S3a, ESI†).[44] These phenomena indicated that the carbonate species were consumed and converted into other reduction products during the hydrogenation process. In addition, the signals for CH_4 and CO_2 were observed successively throughout the TPH process (Fig. S3b, ESI†). Thus, the whole hydrogenation process of K–Pt/$Ni_3Al_1O_x$ involved the reaction in which K_2CO_3 was reduced by H_2 as well.

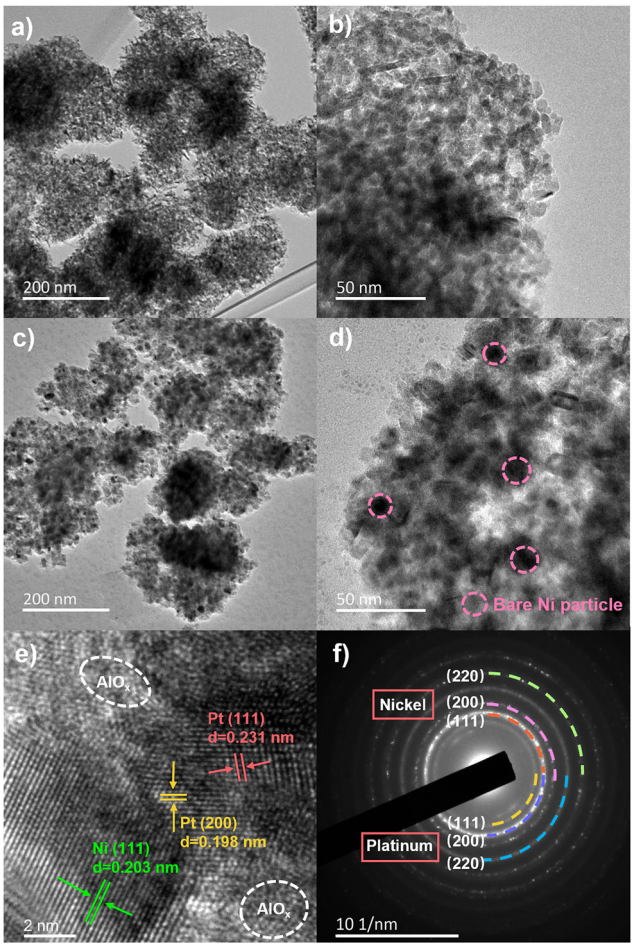

Fig. 2 HR-TEM images of (a) and (b) calcined and (c) and (d) reduced K–Pt/$Ni_3Al_1O_x$, (e) the HR-TEM lattice fringe image and (f) its corresponding SAED image of the K–Pt/$Ni_3Al_1O_x$ R sample.

To investigate the valence state and surface compositions of the materials, X-ray photoelectron spectra of Ni 2p and O 1s regions were obtained for both K–Pt/$Ni_3Al_1O_x$ and K–Pt/$Ni_3Al_1O_x$-R samples (Fig. 1d and e). The Ni $2p_{3/2}$ spectrum was primarily deconvoluted into three contributors, situated at around 854 eV, 856 eV and 860 eV, corresponding to free NiO species, Ni_2AlO_4 species and its shake-up satellite peak, respectively.[45] After reduction, a new peak at approximately 852 eV in the Ni $2p_{3/2}$ spectrum, indicative of Ni^0 formation, was observed,[46] which was consistent with XRD results. However, the Ni^{2+} state persisted in the K–Pt/Ni_3AlO_x-R sample, likely due to surface oxidation during the *ex situ* transfer. Besides, the O 1s spectra were resolved into two main peaks: one corresponding to lattice oxygen (O_α) at around 529 eV, and the other attributed to surface adsorbed oxygen (O_β) at around 531 eV.[45] Oxygen vacancies (O_{vs}) are known to play a crucial role in catalytic reactions, with their relative intensity being positively correlated to the ratio of O_β to $O_\alpha + O_\beta$.[47,48] The ratio of O_β to $O_\alpha + O_\beta$ of the K–Pt/Ni_3AlO_x-R sample (67.5%) is remarkably higher than that of the unreduced K–Pt/Ni_3AlO_x sample (43.4%). This suggested that the reduction treatment enhanced O_{vs} formation, thereby accelerating the catalytic process.[49,50]

The morphology of the calcined and reduced K–Pt/$Ni_3Al_1O_x$ sample was investigated using HR-TEM. Notable morphological changes were observed during the thermal-hydrogenation treatment, with a transition from a fluffy sheet structure (Fig. 2a and b) to granular structure (Fig. 2c and d). This transformation was attributed to the formation of metallic Ni particles after reduction, which is consistent with the XRD results showing the conversion of NiO to Ni^0 after H_2 reduction. Ni particles were well dispersed over the support surface, with no visible agglomeration. Fig. 2e and f showed crystalline lattices with the spacings of 0.203 nm, 0.198 nm, and 0.231 nm, as confirmed by the SAED patterns, which correspond to the (111) planes of metallic Ni and the (200) and (111) planes of metallic Pt. In the meantime, the vague region in Fig. 2e suggests the presence of AlO_x, indicating that Ni nanoparticles are embedded within an amorphous AlO_x matrix. TEM-EDS mapping further illustrated the homogeneous distribution of Ni, Al, O, K, and Pt in the K–Pt/$Ni_3Al_1O_x$ sample (Fig. S4, ESI†).

Due to the high affinity of both CO_2 and NO_x for alkaline substances, they jointly participate in the adsorption process of the CNSR process. The surface basicity is critical for this reaction. Thus, CO_2-TPD and NO-TPD are conducted to evaluate the adsorption capacity of the material for CO_2 and NO_x, as well as the stability of carbonates and nitrates. The influence of H_2 pretreatment and potassium addition on the adsorption and desorption properties of CO_2 and NO was investigated. According to the strength of the interaction between CO_2 and the material, the desorption peaks of CO_2 can be categorized into three zones: weak (<200 °C), intermediate (200–500 °C) and strong (>500 °C) basic sites (Fig. 3a). The weak and moderate interactions play a predominant role in CO_2 methanation and ICCM reactions, whereas strong basic sites interact irreversibly with CO_2, restricting its mobility and thereby hindering the adsorption–dissociation process.[51–53] The results showed that all desorption signals from the tested samples are located in the low-to-medium temperature region, echoing this theory. The CO_2 desorption intensity through the TPD integral area was ranked as follows: K–Pt/$Ni_3Al_1O_x$-R > Pt/$Ni_3Al_1O_x$-R > K–Pt/$Ni_3Al_1O_x$. It is evident that the sample without H_2 treatment exhibited almost no CO_2 adsorption properties. This lack of basic sites primarily derived from the high decomposition temperature of K_2CO_3 in an inert atmosphere, as well as from an insufficiency of metallic sites and oxygen vacancies with a certain capacity for CO_2 adsorption. The significant increase in peak intensity of the after-reduced samples can be attributed to the adsorption sites provided by the metallic surface of the mono- and bimetallic nanoparticles, as well as by surface hydroxyl and oxygen vacancies at the phase interface.[54,55] This suggests that hydrogenation treatment plays a key role in generating adsorption sites. This is consistent with XPS results, which show that more oxygen vacancies are induced in the after-reduced samples.[56,57] In addition, CO_2 desorption was significantly higher for the K–Pt/$Ni_3Al_1O_x$-R samples compared to the sample without potassium, likely due to the additional alkaline sites created by reduced K species in the form of K_2O or KOH.

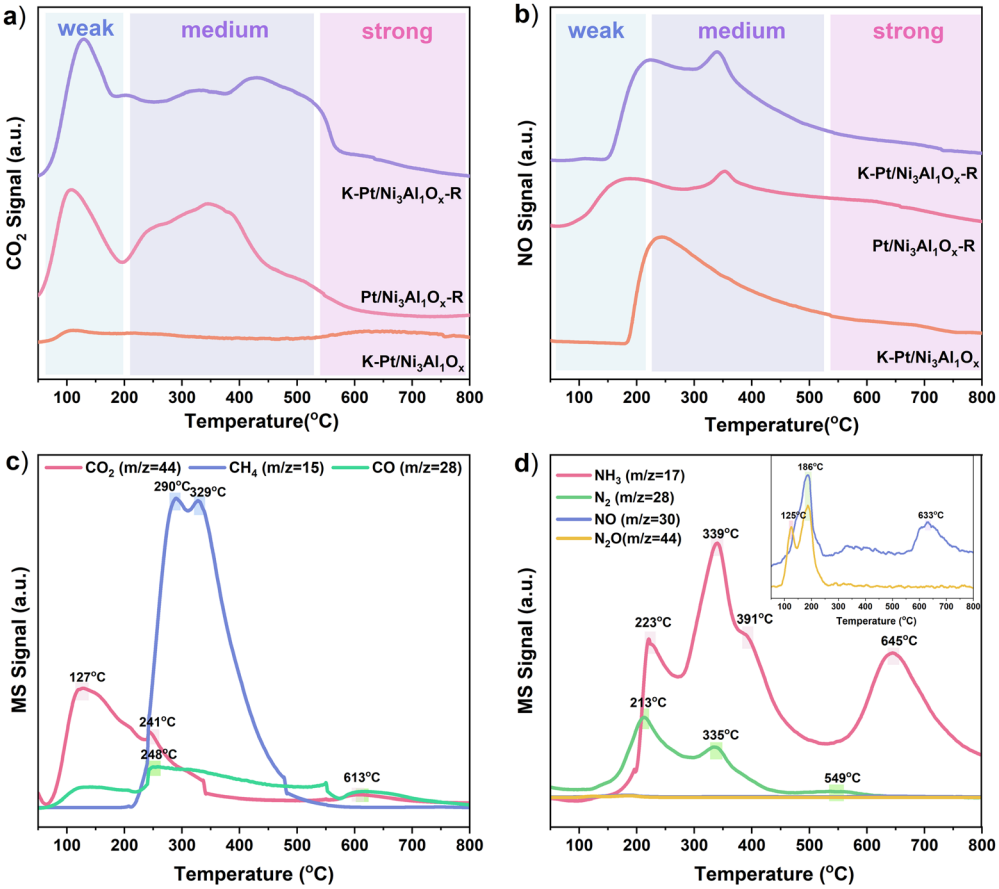

Fig. 3 (a) CO_2-TPD and (b) NO-TPD analyses, (c) the product curve during H_2-TPSR on pre-adsorbed CO_2 and (d) pre-adsorbed NO_x of the K–Pt/$Ni_3Al_1O_x$-R sample.

Similarly, the NO desorption signal can also be divided into three regions using the same criterion as the CO_2-TPD, as depicted in Fig. 3b. The NO desorption occurred in the following descending order: K–Pt/$Ni_3Al_1O_x$-R, K–Pt/$Ni_3Al_1O_x$ and Pt/$Ni_3Al_1O_x$-R. In contrast to CO_2-TPD results, the presence of K species largely facilitates the adsorption properties of NO, whether pretreated or not. A new desorption peak appeared around 350 °C for both reduced samples, suggesting that it may correspond to NO storage on the oxygen vacancies and the active metallic surface. Meanwhile, the increase in peak intensity in the mid-temperature range was in accordance with the temperature range of the CNSR process. Overall, the K addition and H_2 reduction promote NO adsorption capacity jointly.

H_2-TPSR measurements were performed on the K–Pt/$Ni_3Al_1O_x$-R sample after CO_2 or NO_x adsorption to evaluate their reactivity with H_2, as illustrated in Fig. 3c and d. Initially, gaseous CO_2 escaped, which can be attributed to the presence of weakly physisorbed CO_2 in the sample, along with the limited catalytic activity of the Pt and Ni phase at low temperatures, preventing the efficient transformation of CO_2. Subsequently, CH_4 begins to generate at approximately 200 °C, achieving a maximum at around 300 °C, accompanied by the production of minor amounts of by-product CO, implying that CH_4 is the preferred product during the hydrogenation reaction. Furthermore, the wide temperature range for CH_4 production (200–500 °C) may result from the presence of stubborn carbonates that require higher temperatures to react with H_2, which was matched with the CO_2-TPD results.

From the perspective of H_2-TPSR with NO_x, the reaction occurred well below the storage temperature, accompanied by a significant generation of N_2 and NH_3 without pronounced NO_x desorption or N_2O formation, suggesting that the nitrates exhibited superior reactivity with H_2. Within the temperature range of 50 °C to 500 °C, the order of conversion products is N_2O, followed by N_2, and finally NH_3, which correlated with the ratio of H_2 to NO, as explained by reactions (5)–(7). The generation of NH_3 and N_2O at higher temperatures (around 650 °C) resulted from the reduction of recalcitrant nitrates.

$$NO + \frac{1}{2}H_2 \rightarrow \frac{1}{2}N_2O + \frac{1}{2}H_2O \quad (5)$$

$$NO + H_2 \rightarrow \frac{1}{2}N_2 + H_2O \quad (6)$$

$$NO + \frac{5}{2}H_2 \rightarrow NH_3 + H_2O \quad (7)$$

3.2. Performance evaluation of K–Pt/$Ni_3Al_1O_x$ for ICCM and NSR reactions

The separate performance tests for ICCM and NSR reactions were conducted at 350 °C to assess the feasibility of the K–Pt/$Ni_3Al_1O_x$ for both processes. Fig. 4a illustrates the transient gas concentration profiles during the ICCM process. In this reaction, three prime gaseous species: CO_2, CO and H_2O, can be observed throughout the adsorption period. Due to the high CO_2 concentration in the gas cell when stabilizing the mixed gas, the CO_2 signal did not show a trend toward zero. Instead, it decreased to a certain concentration before instantly rising back to the initial value, indicating the saturation of CO_2 capture sites. MS experiments further confirmed the existence of a sustained period of CO_2 penetration on the K–Pt/$Ni_3Al_1O_x$-R sample (Fig. S5, ESI†). This behavior indicated the effective CO_2 adsorption capacity of the material. Except CO_2, minor amounts of CO and H_2O were also detected during the adsorption period. CO was generated *via* the Reverse Water Gas Shift (RWGS) reaction,[58] where CO_2 reacted with H atoms on the reduced surface of the samples. The production of H_2O can occur through various pathways, possibly from the reaction of CO_2 stored on hydrated alkaline sites (KOH), the RWGS reaction between CO_2 and dissociated H atoms, or the reaction of O_2 from the inlet stream with dissociated H atoms.[13,58,59]

In the hydrogenation stage, gaseous CO_2 desorbed first; however, CH_4 formation did not occur initially. This may be due to the oxidation of some surface catalytic sites during adsorption (Ni^0 → NiO), leading to a decrease in catalytic activity. It takes time for the surface to revert to the active metallic state, contributing to the delayed emergence of CH_4. Subsequently, the CH_4 concentration increased rapidly to a maximum, accompanied by only minor CO production. The observed tail-dragging during the decline suggested the presence of various adsorbed CO_2 species and carbonate species within the materials, each exhibiting a different methanation rate. Besides, the delay in H_2O production is due to its pre-adsorption on K_2O or the support, and only appears once these sites become saturated. The production and performance for ICCM are presented in Fig. 4c and Table 1, the CO_2 conversion reached 63.9% with a CH_4 selectivity of up to 97.4%. The performance of ICCM, as reported in the literature, is summarized in Table S3 (ESI†). The ICCM performance is significantly influenced by various operating conditions, including temperature, O_2 presence and concentration, H_2 concentration, and space velocity. For single ICCM performance, the CO_2 conversion in this work is not as high as the best results reported in the literature, due to differing reaction conditions. This limitation primarily arises from CO_2 desorption during the hydrogenation period, which hinders the overall conversion efficiency. However, the key innovation of this study lies in achieving the simultaneous removal of NO_x and CO_2, as well as the utilization of CO_2. In future work, the ICCM performance will be enhanced by optimizing DFMs.

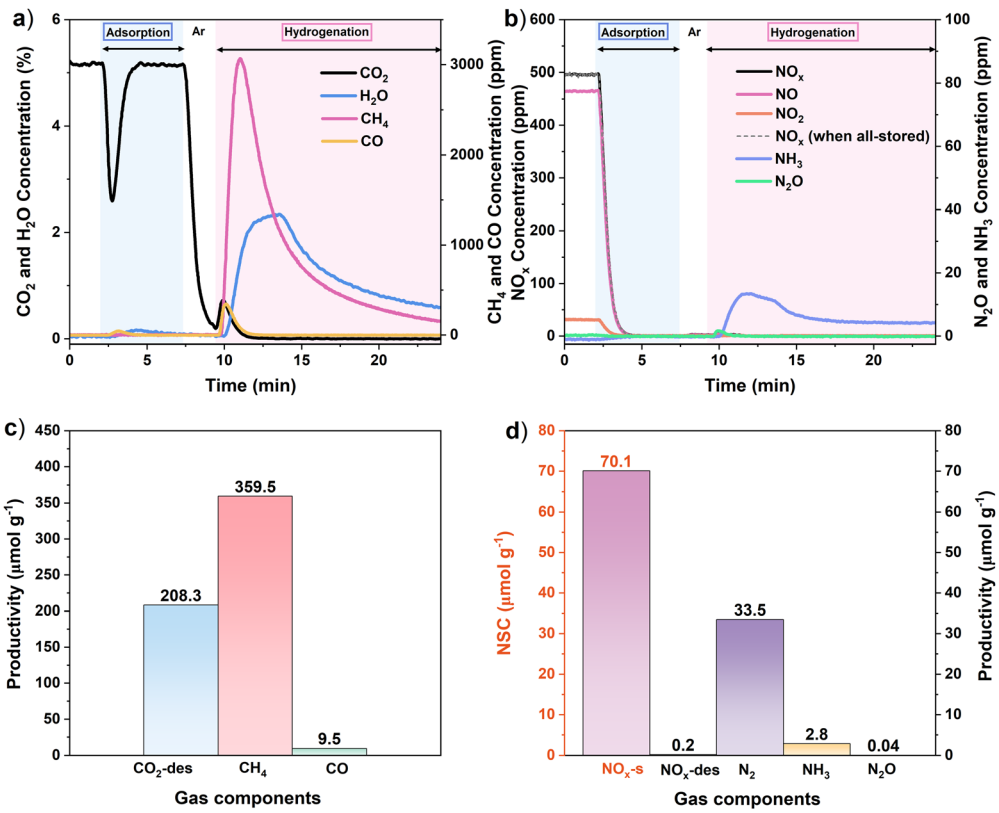

Fig. 4 The transient curves of various gas components and the related performance for (a) and (c) ICCM and (b) and (d) NSR reactions of the K–Pt/$Ni_3Al_1O_x$ sample.

Table 1 Conversion and selectivity performance for independent ICCM and NSR tests

ICCM		NSR	
CO_2 conversion (%)	CH_4 selectivity (%)	NO_x conversion (%)	N_2 selectivity (%)
63.9	97.4	99.7	95.9

For NSR performance of the K–Pt/$Ni_3Al_1O_x$ material, in contrast to CO_2 adsorption, the concentration of inlet NO_x in the adsorption stage rapidly drops to zero, and there was almost no NO_x signal detected during the 5-min storage period, demonstrating that the NO_x storage efficiency (NSE) is close to 100% (Fig. 4b). Furthermore, the desorbed NO_x (NO_x-des) and the yield of N_2O during hydrogenation were negligible (Fig. 4d), which coincides with the previous study: the addition of K^+ significantly enhanced the thermal stability of nitrates and improved the nitrates' reduction activity, thereby suppressing the formation of NO_x-des and N_2O in the hydrogenation period.[60] In the reduction process, although N_2 could not be detected due to equipment limitation, previous studies on the NSR reaction proved that N_2 is likely produced simultaneously with N_2O.[61] As the reaction continues, NH_3 appeared with a wider tail peak and a slower production rate. This is likely due to the reaction between redundant refractory nitrate species and high concentrations of H_2.[62] Almost complete conversion of stored NO_x is achieved during the reduction process, with N_2 selectivity up to 96% (Table 1). Two additional reactions described in eqn (8) and (9) may also occur during the reduction stage, potentially enhancing N_2 generation.

$$N_2O + H_2 \rightarrow N_2 + H_2O \quad (8)$$

$$6KNO_3 + 10NH_3 \rightarrow 8N_2 + 3K_2O + 15H_2O \quad (9)$$

3.3. Performance evaluation of K–Pt/$Ni_3Al_1O_x$ for the innovative CNSR process

The independent performance of ICCM and NSR reactions highlights the function of K–Pt/$Ni_3Al_1O_x$ materials for both reactions, which is crucial for the CNSR process. Given this versatility, K–Pt/$Ni_3Al_1O_x$ was used to evaluate the possibility of the CO_2/NO_x storage and reduction process within a single reactor. The transient profiles of carbon and nitrogen species involved in the CNSR process are illustrated in Fig. 5a and b. Overall, the CNSR process exhibited similarities to both the ICCM and the NSR reactions during the storage and reduction period. In the first (adsorption) stage, a transitory decline of CO_2 and a persistent storage of NO_x occurred accompanied by the generation of a small amount of CO, N_2O and H_2O. During the second (reduction) stage, different gaseous products appeared in the order of CO_2, N_2O, CO, CH_4 and NH_3. In this reaction, NO_x-s was preferentially reduced, as evidenced by the detection of trace amounts of N_2O. The formation of CO_2 hydrogenation products occurred later than that of N_2O. This delay can be attributed to two reasons: (1) oxidation may have inactivated the active sites, hindering the CO_2 reduction process; (2) the reduction of nitrate requires less hydrogen compared to carbonate, which influences the sequence of reactions. The *in situ* DRIFTS results shown in Fig. 8 clearly demonstrate that nitrate or nitrite is preferentially and quickly reduced compared to carbonate. The performance of the CNSR process is illustrated in Fig. 5c and Table 2. The conversions of CO_2 and NO_x were 60.8% and 99.5%, respectively, with excellent CH_4 and N_2 selectivity of 98.9% and 90.3%.

To prove the pivotal role of potassium, the CNSR process was also tested for the Pt/$Ni_3Al_1O_x$ sample without K. The transient curve and performance comparison with K–Pt/$Ni_3Al_1O_x$ are displayed in Fig. S6 and S7 (ESI†). It is evident that the performance of K–Pt/$Ni_3Al_1O_x$ is superior to Pt/$Ni_3Al_1O_x$, particularly in terms of CO_2 capture capacity, CO_2 conversion and NSE. In the adsorption stage, the NO_x concentration increased rapidly after a decline, reaching 290 ppm within 5 min, with an NSE of only 71.1%. This behavior is consistent with the NO-TPD results, further confirming that potassium species are critical for NO adsorption. During the hydrogenation stage, a significant portion of the C-species in Pt/$Ni_3Al_1O_x$ samples was released as gaseous CO_2, rather than being converted into CH_4 or CO, resulting in a lower CO_2 conversion (18.8%). This observation underscores the pivotal role of potassium in the CNSR process.

Furthermore, the effect of water vapor (5 vol%) on the CNSR process was investigated, the results are shown in Fig. 6 and Table 2. It was observed that the introduction of H_2O primarily restricted the adsorption of CO_2 and NO_x. The CO_2 capture capability and NO_x storage capacity decreased from 665.4 μmol g^{-1} and 64.5 μmol g^{-1} to 541.6 μmol g^{-1} and 61.1 μmol g^{-1}, respectively. Whereas, the CO_2 and NO_x conversion (63% and 99.7%) as well as CH_4 and N_2 selectivity (97% and 97.2%) remained relatively stable. The above results demonstrated that the integrated approach for CO_2/NO_x storage and reduction can be effectively realized within a single reactor. This not only highlights the distinct advantages of K–Pt/$Ni_3Al_1O_x$ material but also opens avenues for further optimization and application in multi-pollution control technologies.

3.4. Cycling performance of K–Pt/$Ni_3Al_1O_x$ for the CNSR process

Reusability of the materials is crucial for the economic viability of any catalytic process. Herein, cycling tests based on the CNSR process were conducted to evaluate the stability of the K–Pt/$Ni_3Al_1O_x$ DFM. It is noted that the single CNSR tests aimed to provide a comprehensive understanding of the overall behavior of the CNSR process, allowing for a thorough assessment of CO_2 and NO_x storage and reduction capabilities. However, this condition of long-time adsorption and hydrogenation do not accurately reflect the practical requirements of industrial applications. Therefore, relatively shorter intervals were applied to storage (3 min) and reduction (5 min) for the cycling test. The results of the cyclic tests will provide valuable insights into the material's longevity and its potential for sustained performance in real working conditions.

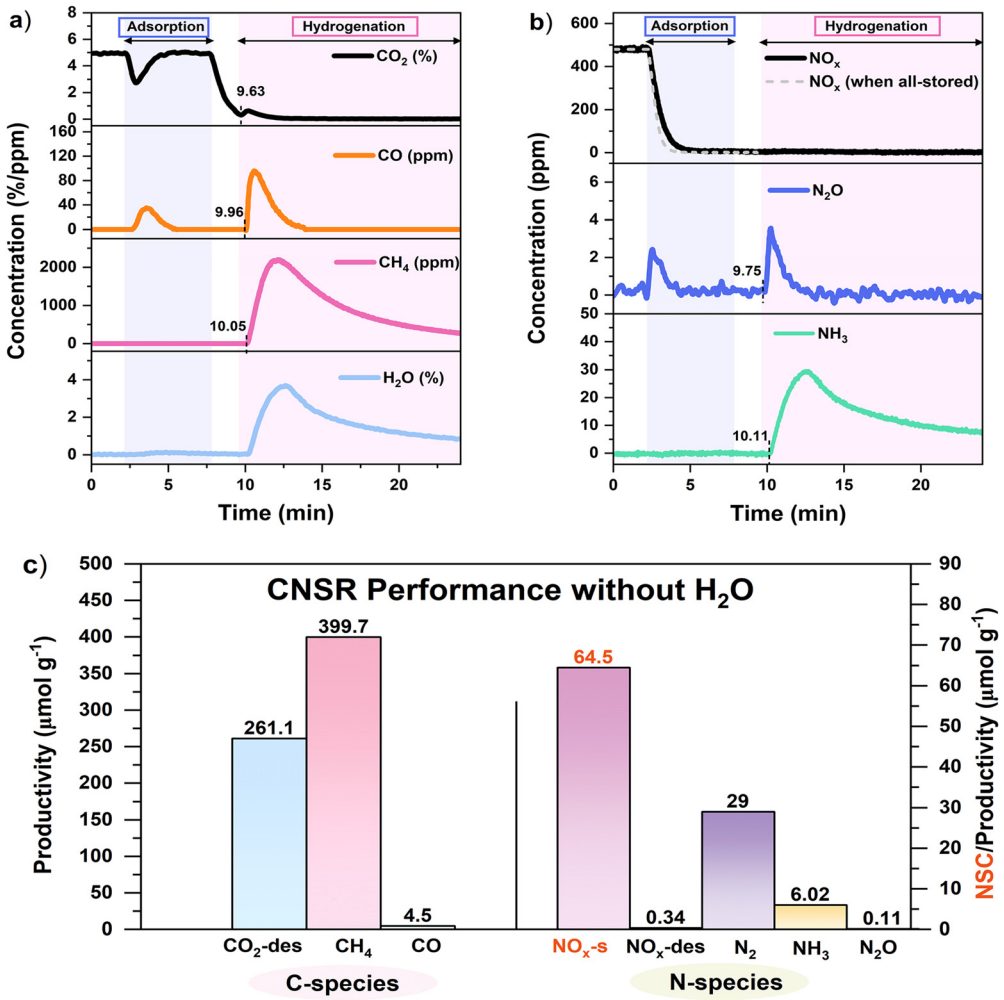

Fig. 5 The instantaneous concentration profiles of each gaseous component: (a) C-species and H_2O, (b) N species, and (c) the productivity of the CNSR reaction for the K–Pt/$Ni_3Al_1O_x$ sample.

Table 2 The related performance for the integrated CNSR process under different conditions

CNSR performance	C_{CO_2}[a] (μmol g^{-1})	NSC[b] (μmol g^{-1})	CO_2 Conv. (%)	CH_4 Sel. (%)	NO_x Conv. (%)	N_2 Sel. (%)	NSE[c] (%)
Pt/$Ni_3Al_1O_x$ (without H_2O)	310.2	49.7	18.8	90.8	98.2	93.6	71.1
K–Pt/$Ni_3Al_1O_x$ (without H_2O)	665.4	64.5	60.8	98.9	99.5	90.3	94.3
K–Pt/$Ni_3Al_1O_x$ (with H_2O)	541.6	61.1	63.0	97.0	99.7	96.1	89.2

[a] Captured CO_2 during the adsorption period, calculated using eqn (S9) (ESI). [b] Stored NO_x during the adsorption period, calculated using eqn (S1) (ESI). [c] NO_x storage efficiency calculated using eqn (S10) (ESI).

Fig. 7 and Fig. S8 (ESI†) show the cycling performance and the dynamic airflow concentration curves of all involved gases over 10 cycles for the K–Pt/$Ni_3Al_1O_x$ sample. Surprisingly, CO_2 conversion exhibited a remarkable increase, rising from 41.5% in the first cycle to 66% in the last cycle. In conjunction with CO_2-TPD (Fig. 3a), this improvement may be attributed to the presence of medium-strong alkaline sites (350–500 °C), which result in a portion of the CO_2 being tightly bound to the material during the initial adsorption process. The CO_2 capture capacity for each cycle is recorded in Table S4 (ESI†). After the first cycle, the amount of CO_2 adsorbed decreased and stabilized, with its corresponding desorption during the hydrogenation stage also decreasing, stabilizing at approximately 110 μmol g^{-1} from the initial 309 μmol g^{-1}. Meanwhile, the production of CH_4 remained relatively constant, yielding about 195 μmol g^{-1} after a slight decrease during the first cycle. Thus, the CO_2 conversion improved somewhat. Although there was a slight increase in CO as a by-product of the hydrogenation process, the amount of CO produced was much lower than that of CH_4 and had an insignificant effect on the selectivity of CH_4. Consequently, CH_4 selectivity remained consistently above 90% throughout all 10 cycles. This performance underscores the

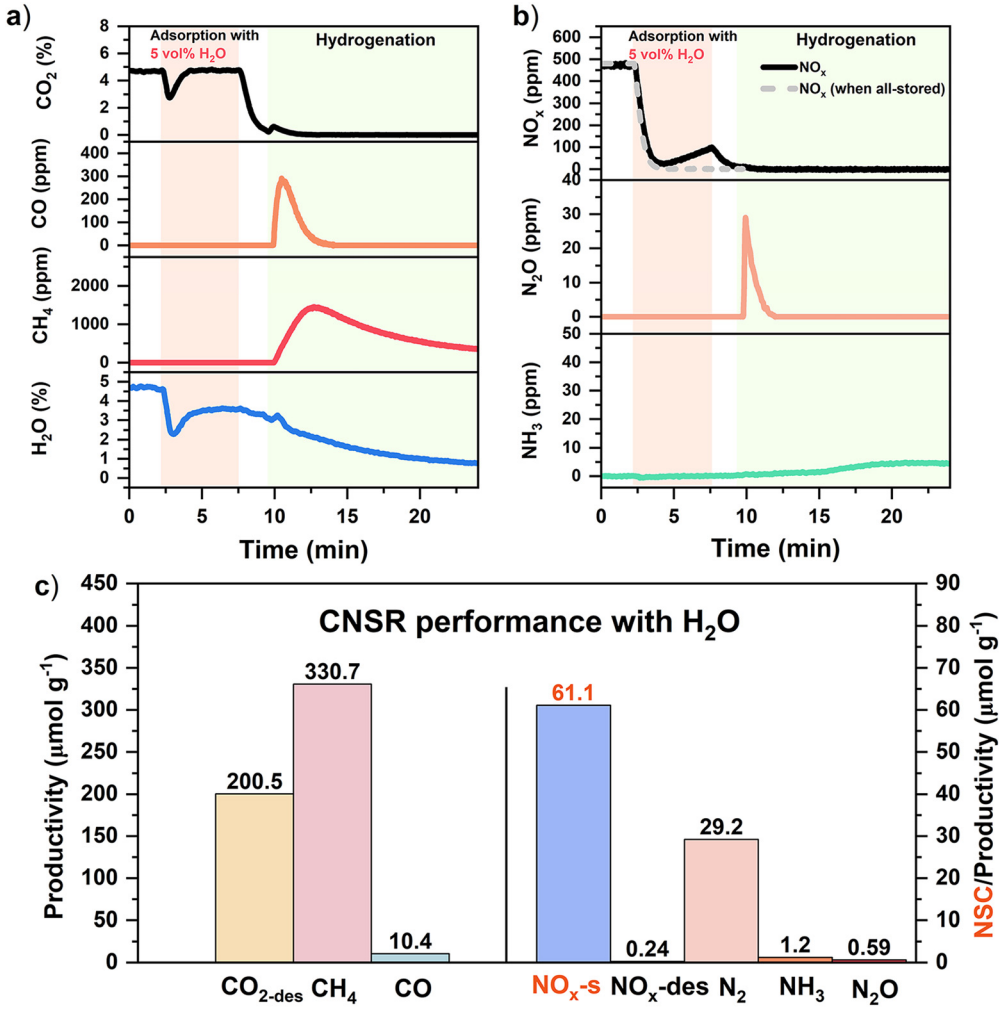

Fig. 6 The CNSR transient profiles (under 5-min adsorption period with 5 vol% H_2O): (a) C-species and H_2O, (b) N species, and (c) the productivity of the CNSR process for the K–Pt/$Ni_3Al_1O_x$ sample.

stability and effectiveness of K–Pt/$Ni_3Al_1O_x$ in the CNSR process, showcasing its potential for practical applications in CO_2/NO_x storage and reduction systems.

In terms of NO_x, the conversion is basically unchanged at close to 100%. However, N_2 selectivity decreased during the cycle test, from 97.4% in the first cycle to 81.2% by the tenth cycle. Combined with the trend observed in the dynamic curves (Fig. S8, ESI†), as the number of cycles increased, a higher concentration of NO_x was detected at the end of adsorption period, indicating a reduced capability of the K–Pt/$Ni_3Al_1O_x$ to store NO_x. Furthermore, measurements indicated that more NO_x-des, N_2O, and NH_3 were generated during the hydrogenation over the ten cycles. However, the production of NO_x-des and N_2O stabilized at low levels, rendering them negligible. In contrast, NH_3 showed a continuous upward trend throughout the cycles, which was identified as the primary factor contributing to the decline in N_2 selectivity.

Comprehensively, the novel concept for CO_2/NO_x storage and reduction is feasible with the developed K–Pt/$Ni_3Al_1O_x$ material, but further optimization of its composition and structure is essential to enhance both stability and performance in the CNSR process.

3.5. Mechanism studies of the CNSR process over K–Pt/$Ni_3Al_1O_x$

To better understand the changes in surface species, particularly carbonate and nitrate, as well as the reduction order, *in situ* DRIFTS tests were performed. Since the IR spectral regions of nitrate/nitrite and carbonate partially overlap, the ICCM and NSR processes was first conducted. When the K–Pt/$Ni_3Al_1O_x$-R sample is exposed to CO_2, three bands appear at approximately 1605 cm^{-1}, 1330 cm^{-1}, and 1068 cm^{-1} (Fig. 8a). The bands at 1605 cm^{-1} and 1330 cm^{-1} are generally assigned to carboxylate ions[63] or bidentate carbonate,[64,65] while the weaker band at 1068 cm^{-1} is associated with the symmetric stretching vibration of carbonate groups.[66] These spectral features are indicative of carbonate species formed on the potassium phase.[67] The intensity of the carbonate bands remains nearly unchanged after 3 minutes of adsorption, indicating CO_2 adsorption saturation. After an Ar purge

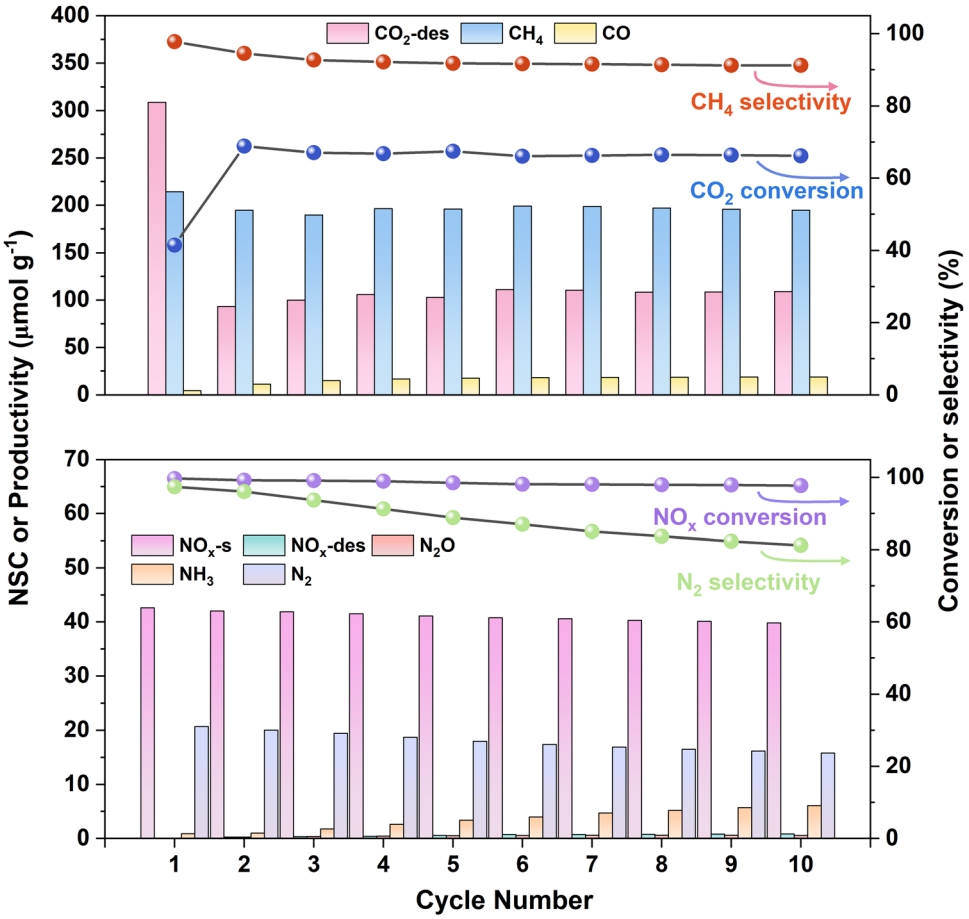

Fig. 7 The cyclic CNSR performance over the K–Pt/$Ni_3Al_1O_x$ material at 350 °C.

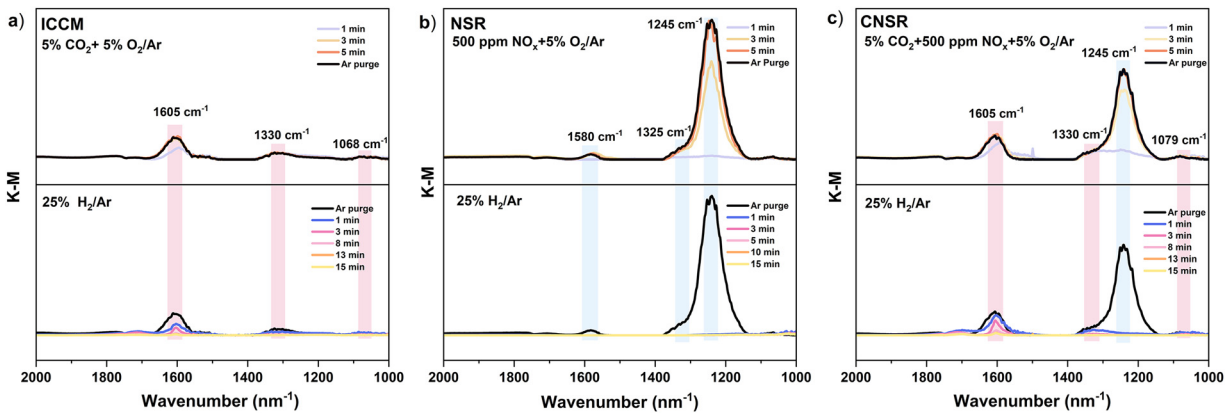

Fig. 8 *In situ* DRIFTS of the (a) ICCM (b) NSR, and (c) CNSR process for the K–Pt/$Ni_3Al_1O_x$-R sample.

(2 minutes), the peaks persist, suggesting that the carbonate species adsorbed on the sample are not easily removed by Ar. During the hydrogenation period, the carbonate peak intensity gradually decreases and returns to baseline after 15 minutes, indicating complete conversion of the carbonate. Similarly, for the NSR process (Fig. 8b), the formation of both nitrate (1580 cm^{-1} and 1245 cm^{-1}) and nitrite (1325 cm^{-1}) was observed during the adsorption period.[68] The intensity of these nitrate/nitrite bands increased steadily over 5 minutes, indicating continuous storage of NO_x in the sample. During the hydrogenation stage, these bands completely vanished within 1 minute, signifying full transformation of the stored NO_x. A similar process of CO_2 and NO_x storage and reduction is shown in Fig. 8c. The IR spectral changes align well with the transient

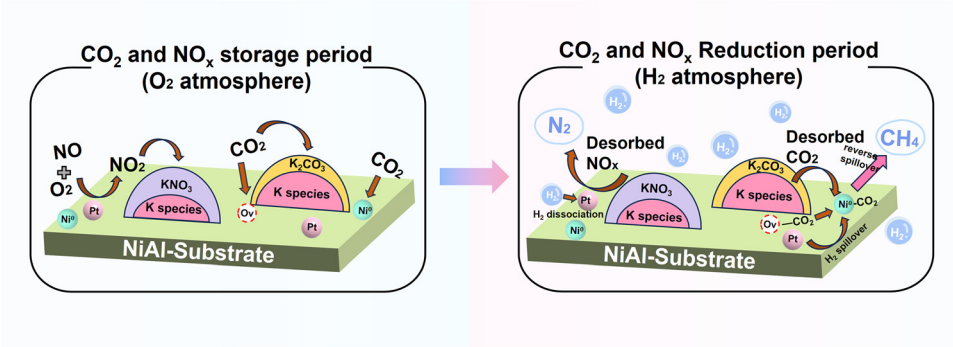

Fig. 9 The proposed reaction mechanisms of the CNSR process over K–Pt/$Ni_3Al_1O_x$.

profiles of the CNSR process, indicating that CO_2 reached saturation more easily than NO_x, and that stored NO_x is reduced easier/faster than captured CO_2 during the hydrogenation stage.

Based on the characterization and performance results, along with the mechanism reported in the literature for NSR and ICCM reactions,[59,69,70] a speculative mechanism for the CNSR process over the K–Pt/$Ni_3Al_1O_x$ material has been proposed, as depicted in Fig. 9. In the CO_2 and NO_x storage period: first, NO is partially oxidized to NO_2 *via* precious metals (Pt). The formed NO_2, along with CO_2, is stored on various active sites (alkali metal, reducible transition metal and oxygen vacancies). During the CO_2 and NO_x reduction period: hydrogen is injected into the system, where it dissociates on the active components. The stored carbonates and nitrates or nitrites on adsorption sites were decomposed and released in the form of NO_x and CO_2 gas. Finally, NO_x is reduced to N_2 through hydrogenation, while CO_2 is converted to CH_4.

This mechanism highlights the synergistic roles of precious metals, alkali metals, and transition metals in facilitating the CNSR process. At the commencement of the first stage, metallic Pt played a critical role in NO oxidation. This conversion significantly enhanced the NO_x storage capacity, as evidenced by numerous studies on NSR. Subsequently, both NO_x and CO_2 are stored on various adsorption sites. These sites are not limited to alkali metal, they also include the surface of reducible transition metal and oxygen vacancies.

At the beginning of the hydrogenation period, a part of Ni and Pt oxides formed during the storage stage are reduced primarily, accompanied by heat release. This heat release accelerates the decomposition of stored carbonates and nitrates. The reduction process may involve two spillover mechanisms.[71] The first is hydrogen dissociates at the Pt and Ni sites, and then migrates to the adsorption sites where it reacts with CO_2 and NO. An alternative mechanism involves the reverse spillover of desorbed CO_2 and NO from storage sites to the Ni^0 and Pt^0 phase, where they react with dissociated H atoms on active metallic phases. This mechanism may dominate in the initial stage of hydrogenation, as the desorption of CO_2 and NO is observed at the onset of H_2 injection. This observation suggested that while CO_2 and NO are in motion, there are insufficient active sites for immediate conversion, allowing them to escape and be detected as raw gaseous forms. As hydrogenation continues, both mechanisms coexist. However, at a later stage of the reaction, the presence of hard-to-decompose carbonates and nitrates caused positive spillover to become the dominant mechanism until these compounds are completely consumed.

4. Conclusions

In this contribution, we proposed a new concept, named CO_2/NO_x storage and reduction (CNSR), for the purpose of simultaneous removal of CO_2 and NO_x from flue gases. This approach allows for the disposal of two pollutants in a single reactor, circumventing the energy consumption and economic losses associated with separated devices and temperature-swing processes. A novel dual functional material (DFM) K–Pt/$Ni_3Al_1O_x$ was also designed for the innovative CNSR process. The separate ICCM and NSR tests suggest that it is applicable for CO_2 reduction to CH_4 as well as NO_x storage and reduction to N_2. More importantly, the integrated CNSR tests presented good performance. The CO_2 and NO_x conversions were 60.8% and 99.5%, with a CH_4 and N_2 selectivity of 98.9% and 90.3%, respectively. Although water vapor competed with CO_2 and NO_x for adsorption, reducing their capture capacity, it did not affect the conversions of CO_2 and NO_x. Additionally, after 10 cycles, the K–Pt/$Ni_3Al_1O_x$ material exhibited a stable CH_4 yield of about 195 μmol g^{-1}, with a CO_2 conversion around 66% and a CH_4 selectivity above 90%. Besides, the conversion of NO_x is basically unchanged at close to 100%. Although slight declines in NO_x storage capacity and N_2 selectivity were observed, the N_2 selectivity was still 81.2% after 10 cycles. Finally, the speculative mechanisms for the CNSR process over K–Pt/$Ni_3Al_1O_x$ material were revealed.

However, challenges remain, and in future investigations, two aspects can be further explored for the CNSR process: (1) the design and development of high performance DFMs, especially those with high CO_2 adsorption and conversion performance; (2) the impacts of potential flue gas components, including CO and SO_2, and others. With the development of high-performance materials, CNSR has the potential to become a promising solution for pollutants and CO_2 capture and conversion.

Author contributions

Jiaqi Wei: formal analysis; investigation; validation; writing – original draft. Yanshan Gao: supervision; resources; funding acquisition; writing – review & editing. Cheng Zhang: formal analysis; investigation. Qiang Wang: conceptualization; supervision; resources; funding acquisition; writing – review & editing.

Data availability

The data supporting the findings of this study are available within the paper and its ESI.†

Conflicts of interest

There are no conflicts of interest to declare.

Acknowledgements

We acknowledge the National Natural Science Foundation of China (52225003, 52270099), and the 5·5 Engineering Research & Innovation Team Project of Beijing Forestry University (BLRC2023B04).

References

1 S. Li, S. Wang, Q. Wu, Y. Zhang, D. Ouyang, H. Zheng, L. Han, X. Qiu, Y. Wen, M. Liu, Y. Jiang, D. Yin, K. Liu, B. Zhao, S. Zhang, Y. Wu and J. Hao, *Earth System Sci. Data*, 2023, **15**, 2279–2294.
2 S. D. Musa, T. Zhonghua, A. O. Ibrahim and M. Habib, *Renewable Sustainable Energy Rev.*, 2018, **81**, 2281–2290.
3 Y. Hou, Y. Chen, X. He, F. Wang, Q. Cai and B. Shen, *Chem. Eng. J.*, 2024, **490**, 151424.
4 A. Islam, S. H. Teo, C. H. Ng, Y. H. Taufiq-Yap, S. Y. T. Choong and M. R. Awual, *Prog. Mater. Sci.*, 2023, **132**, 101033.
5 P. Granger and V. I. Parvulescu, *Chem. Rev.*, 2011, **111**, 3155–3207.
6 L. Han, S. Cai, M. Gao, J.-Y. Hasegawa, P. Wang, J. Zhang, L. Shi and D. Zhang, *Chem. Rev.*, 2019, **119**, 10916–10976.
7 Y. Li, D. Chen, X. Xu, X. Wang, R. Kang, M. Fu, Y. Guo, P. Chen, Y. Li and D. Ye, *Environ. Sci. Technol.*, 2023, **57**, 3467–3485.
8 G. Liu, H. Zhang, Y. Li, P. Wang and S. Zhan, *EES Catal.*, 2024, **2**, 231–252.
9 N. Takahashi, H. Shinjoh, T. Iijima, T. Suzuki, K. Yamazaki, K. Yokota, H. Suzuki, N. Miyoshi, S.-I. Matsumoto, T. Tanizawa, T. Tanaka, S.-S. Tateishi and K. Kasahara, *Catal. Today*, 1996, **27**, 63–69.
10 M. S. Duyar, M. A. A. Treviño and R. J. Farrauto, *Appl. Catal., B*, 2015, **168–169**, 370–376.
11 Z. Lv, H. Du, S. Xu, T. Deng, J. Ruan and C. Qin, *Appl. Energy*, 2024, **355**, 122242.
12 M. E. Boot-Handford, J. C. Abanades, E. J. Anthony, M. J. Blunt, S. Brandani, N. Mac Dowell, J. R. Fernandez, M. C. Ferrari, R. Gross, J. P. Hallett, R. S. Haszeldine, P. Heptonstall, A. Lyngfelt, Z. Makuch, E. Mangano, R. T. J. Porter, M. Pourkashanian, G. T. Rochelle, N. Shah, J. G. Yao and P. S. Fennell, *Energy Environ. Sci.*, 2014, **7**, 130–189.
13 A. Porta, C. G. Visconti, L. Castoldi, R. Matarrese, C. Jeong-Potter, R. Farrauto and L. Lietti, *Appl. Catal., B*, 2021, **283**, 119654.
14 S. Cimino, E. M. Cepollaro and L. Lisi, *Appl. Catal., B*, 2022, **317**, 121705.
15 S. Cimino, E. M. Cepollaro, M. Pazzi and L. Lisi, *Catal. Today*, 2024, **426**, 114366.
16 X. Zhao, J. Hu, B. Zong, Y. Zhang and C. Wu, *Appl. Catal., B*, 2025, **361**, 124623.
17 L. Li, S. Miyazaki, S. Yasumura, K. W. Ting, T. Toyao, Z. Maeno and K.-I. Shimizu, *ACS Catal.*, 2022, **12**, 2639–2650.
18 S. Sun, Y. Wang, Y. Xu, H. Sun, X. Zhao, Y. Zhang, X. Yang, X. Bie, M. Wu, C. Zhang, Y. Zhu, Y. Xu, H. Zhou and C. Wu, *Appl. Catal., B*, 2024, **348**, 123838.
19 J. Kothandaraman, J. S. Lopez, Y. Jiang, E. D. Walter, S. D. Burton, R. A. Dagle and D. J. Heldebrant, *Adv. Energy Mater.*, 2022, **12**, 2202369.
20 R. Sen, A. Goeppert, S. Kar and G. K. S. Prakash, *J. Am. Chem. Soc.*, 2020, **142**, 4544–4549.
21 H. Sun, S. Sun, T. Liu, J. Zeng, Y. Wang, Z. Yan and C. Wu, *ACS Catal.*, 2024, **14**, 15572–15589.
22 L. Castoldi, L. Lietti, P. Forzatti, S. Morandi, G. Ghiotti and F. Vindigni, *J. Catal.*, 2010, **276**, 335–350.
23 H. P. Nguyen, S. P. Del Valle and O. Marie, *Appl. Catal., B*, 2018, **231**, 391–399.
24 O. E. Medina, A. A. Amell, D. Lopez and A. Santamaria, *Renewable Sustainable Energy Rev.*, 2025, **207**, 114926.
25 Z. Boukha, A. Bermejo-Lopez, U. De-La-Torre and J. R. Gonzalez-Velasco, *Appl. Catal., B*, 2023, **338**, 122989.
26 X. Wu, R. Chang, M. Tan, L. Tao, Q. Fan, X. Hu, H. L. Tan, M. Ahlen, O. Cheung and W. Liu, *Appl. Catal., B*, 2023, **338**, 123053.
27 X. Su, J. Xu, B. Liang, H. Duan, B. Hou and Y. Huang, *J. Energy Chem.*, 2016, **25**, 553–565.
28 X. Wang, D. Hu, Y. Hao, L. Zhang, N. Sun and W. Wei, *Sep. Purif. Technol.*, 2023, **322**, 124295.
29 M. A. Arellano-Trevino, N. Kanani, C. W. Jeong-Potter and R. J. Farrauto, *Chem. Eng. J.*, 2019, **375**, 121953.
30 S. K. Beaumont, S. Alayoglu, C. Specht, W. D. Michalak, V. V. Pushkarev, J. Guo, N. Kruse and G. A. Somorjai, *J. Am. Chem. Soc.*, 2014, **136**, 9898–9901.
31 S. Roy and A. Baiker, *Chem. Rev.*, 2009, **109**, 4054–4091.
32 A. Hanif, M. Sun, S. Shang, Y. Tian, A. C. K. Yip, Y. S. Ok, I. K. M. Yu, D. C. W. Tsang, Q. Gu and J. Shan, *J. Hazard. Mater.*, 2019, **374**, 365–371.
33 Q. Wang and D. O'Hare, *Chem. Rev.*, 2012, **112**, 4124–4155.
34 D. Wierzbicki, R. Baran, R. Debek, M. Motak, T. Grzybek, M. E. Galvez and P. Da Costa, *Int. J. Hydrogen Energy*, 2017, **42**, 23548–23555.

35 Z. Zhou, N. Sun, B. Wang, Z. Han, S. Cao, D. Hu, T. Zhu, Q. Shen and W. Wei, *ChemSusChem*, 2020, **13**, 360–368.
36 R. Yang, Y. Cui, Q. Yan, C. Zhang, L. Qiu, D. O'Hare and Q. Wang, *Chem. Eng. J.*, 2017, **326**, 656–666.
37 Z. Xu, N. Wang, W. Chu, J. Deng and S. Luo, *Catal. Sci. Technol.*, 2015, **5**, 1588.
38 L. He, Q. Lin, Y. Liu and Y. Huang, *J. Energy Chem.*, 2014, **23**, 587–592.
39 Y. Guo, S. Mei, K. Yuan, D.-J. Wang, H.-C. Liu, C.-H. Yan and Y.-W. Zhang, *ACS Catal.*, 2018, **8**, 6203–6215.
40 A. Bermejo-Lopez, B. Pereda-Ayo, J. A. Gonzalez-Marcos and J. R. Gonzalez-Velasco, *Appl. Catal., B*, 2019, **256**, 117845.
41 K. Coenen, F. Gallucci, B. Mezari, E. Hensen and M. van Sint Annaland, *J. CO_2* Util., 2018, **24**, 228–239.
42 J. Tian, P. Zheng, T. Zhang, Z. Han, W. Xu, F. Gu, F. Wang, Z. Zhang, Z. Zhong, F. Su and G. Xu, *Appl. Catal., B*, 2023, **339**, 123121.
43 K. Wang, Z. Hu, P. Yu, A. M. Balu, K. Li, L. Li, L. Zeng, C. Zhang, R. Luque, K. Yan and H. Luo, *Nano-Micro Lett.*, 2024, **16**, 5.
44 C.-X. Wang, H.-X. Liu, H. Gu, J.-Y. Li, X.-M. Lai, X.-P. Fu, W.-W. Wang, Q. Fu, F. R. Wang, C. Ma and C.-J. Jia, *Nat. Commun.*, 2024, **15**, 8290.
45 Z. Wang, T. Zhang, T. R. Reina, L. Huang, W. Xie, N. M. Musyoka, B. Oboirien and Q. Wang, *Fuel*, 2024, **366**, 131383.
46 D. He, S. Wu, X. Cao, D. Chen, L. Zhang, Y. Zhang and Y. Luo, *Appl. Catal., B*, 2024, **346**, 123728.
47 F. He, J. Zhuang, B. Lu, X. Liu, J. Zhang, F. Gu, M. Zhu, J. Xu, Z. Zhong, G. Xu and F. Su, *Appl. Catal., B*, 2021, **293**, 120218.
48 H. Zheng, W. Liao, J. Ding, F. Xu, A. Jia, W. Huang and Z. Zhang, *ACS Catal.*, 2022, **12**, 15451–15462.
49 P. Huang, J. Chu, J. Fu, J. Yu, S. Li, Y. Guo, C. Zhao and J. Liu, *Chem. Eng. J.*, 2023, **467**, 143431.
50 J. Dong, D. Li, Y. Zhang, P. Chang and Q. Jin, *J. Catal.*, 2022, **407**, 174–185.
51 J. Ren, C. Mebrahtu, L. van Koppen, F. Martinovic, J. P. Hofmann, E. J. M. Hensen and R. Palkovits, *Chem. Eng. J.*, 2021, **426**, 131760.
52 Y. Yan, Y. Dai, Y. Yang and A. A. Lapkin, *Appl. Catal., B*, 2018, **237**, 504–512.
53 L. Chen, D. Liu and G. Wei, *Energy Convers. Manage.*, 2024, **299**, 117811.
54 A. I. Tsiotsias, N. D. Charisiou, E. Harkou, S. Hafeez, G. Manos, A. Constantinou, A. G. S. Hussien, A. A. Dabbawala, V. Sebastian, S. J. Hinder, M. A. Baker, K. Polychronopoulou and M. A. Goula, *Appl. Catal., B*, 2022, **318**, 121836.
55 G. I. Siakavelas, N. D. Charisiou, S. AlKhoori, A. A. AlKhoori, V. Sebastian, S. J. Hinder, M. A. Baker, I. V. Yentekakis, K. Polychronopoulou and M. A. Goula, *Appl. Catal., B*, 2021, **282**, 119562.
56 R. Wu, L. Li, Z. Lu, C. Sun, L. Cheng, R. Ye, R. Zhang, Q. Li and G. Feng, *J. Catal.*, 2024, **434**, 115502.
57 X. Yan, C. Duan, S. Yu, B. Dai, C. Sun and H. Chu, *J. CO_2* Util., 2024, **79**, 102648.
58 A. Bermejo-Lopez, B. Pereda-Ayo, J. A. Gonzalez-Marcos and J. R. Gonzalez-Velasco, *J. CO_2* Util., 2019, **34**, 576–587.
59 A. Bermejo-Lopez, B. Pereda-Ayo, J. A. Gonzalez-Marcos and J. R. Gonzalez-Velasco, *Appl. Catal., B*, 2019, **256**, 117845.
60 Z. Bai, B. Chen, Q. Zhao, C. Shi and M. Crocker, *Appl. Catal., B*, 2019, **249**, 333–345.
61 C. Zhang, C. M. Damaskinos, M. A. Vasiliades, Y. Liu, Q. Jiang, Q. Wang and A. M. Efstathiou, *Appl. Catal., B*, 2023, **327**, 122455.
62 I. Nova, L. Lietti, L. Castoldi, E. Tronconi and P. Forzatti, *J. Catal.*, 2006, **239**, 244–254.
63 T. J. Toops, D. B. Smith and W. P. Partridge, *Appl. Catal., B*, 2005, **58**, 245–254.
64 X. Zhu, C. Chen, Q. Wang, Y. Shi, D. O'Hare and N. Cai, *Chem. Eng. J.*, 2019, **366**, 181–191.
65 T. Montanari, L. Castoldi, L. Lietti and G. Busca, *Appl. Catal., B*, 2011, **400**, 61–69.
66 L. Azancot, L. F. Bobadilla, M. A. Centeno and J. A. Odriozola, *Appl. Catal., B*, 2021, **285**, 119822.
67 F. Prinetto, M. Manzoli, S. Morandi, F. Frola, G. Ghiotti, L. Castoldi, L. Lietti and P. Forzatti, *J. Phys. Chem. C*, 2010, **114**, 1127–1138.
68 Z. Say, M. Dogac, E. I. Vovk, Y. E. Kalay, C. H. Kim, W. Li and E. Ozensoy, *Appl. Catal., B*, 2014, **154**, 51–61.
69 L. Castoldi, R. Matarrese, S. Morandi, L. Righini and L. Lietti, *Appl. Catal., B*, 2018, **224**, 249–263.
70 L.-P. Merkouri, L. F. Bobadilla, J. L. Martin-Espejo, J. A. Odriozola, A. Penkova, G. Torres-Sempere, M. Short, T. R. Reina and M. S. Duyar, *Appl. Catal., B*, 2025, **361**, 124610.
71 N. W. Cant, I. O. Y. Liu and M. J. Patterson, *J. Catal.*, 2006, **243**, 309–317.